

Precision Hand Assembly of MEMS Subsystems Using DRIE-Patterned Deflection Spring Structures: An Example of an Out-of-Plane Substrate Assembly

Luis Fernando Velásquez-García, Akintunde Ibitayo Akinwande, *Member, IEEE*, and Manuel Martínez-Sánchez

Abstract—This paper describes a packaging concept for precise hand-assembly of microelectromechanical systems (MEMS) subsystems that uses mesoscaled deep-reactive ion etching (DRIE) patterned passive deflection spring clusters. The method is intended for applications that require decoupling of subsystem process flows to simplify device fabrication in order to attain macro three-dimensionality, or for cases where the device requires spatially referenced macro- and microfeatures with good precision. The design considerations for the deflection springs are presented, and a simple reduced-order model of the expected elastic behavior is proposed. The assembly concept is demonstrated with an electro spray array test structure. This test structure assembles perpendicularly two wafer substrates. The performance of the test structure is benchmarked using finite-element simulations and by measurements of the misalignment introduced by the assembly. A floor for the ultimate alignment accuracy of the assembly concept is proposed. [1456]

Index Terms—Deep-reactive ion etching (DRIE) patterned springs, low-pressure low-temperature die-level packaging, out-of-plane wafer assembly, passive deflection spring assembly, system integration.

I. INTRODUCTION, GOAL, AND MOTIVATION

MICROELECTROMECHANICAL systems (MEMS) take advantage of the set of technologies developed by the semiconductor industry. In the majority of cases, these technologies imply the deposition or removal of layers of material where a planar layout is directly involved via a photolithographic process [1], [2]. The use of in-plane layouts to build structures restricts the range of geometries that can be implemented as part of a micromachine, in particular the aspect ratio and three-dimensionality of MEMS parts. Most of the efforts for photolithographic processes focus on reduction of

Manuscript received November 4, 2004; revised November 5, 2006. This work was supported by the Air Force Office of Scientific Research (AFOSR) under Grant F49620-01-1-0398 and by the Defense Advanced Research Projects Agency under the Micro Gas Analyzer program BAA 03-40. Subject Editor N. C. Tien.

L. F. Velásquez-García is with the Microsystems Technology Laboratories, Massachusetts Institute of Technology, Cambridge, MA 02139 USA (e-mail: lfvelasq@mit.edu).

A. I. Akinwande is with the Department of Electrical Engineering and Computer Science, Massachusetts Institute of Technology, Cambridge, MA 02139 USA (e-mail: akinwand@mtl.mit.edu).

M. Martínez-Sánchez is with the Department of Aeronautics and Astronautics, Massachusetts Institute of Technology, Cambridge, MA 02139 USA (e-mail: mmart@mit.edu).

Color versions of one or more of the figures in this paper are available online at <http://ieeexplore.ieee.org>.

Digital Object Identifier 10.1109/JMEMS.2007.892931

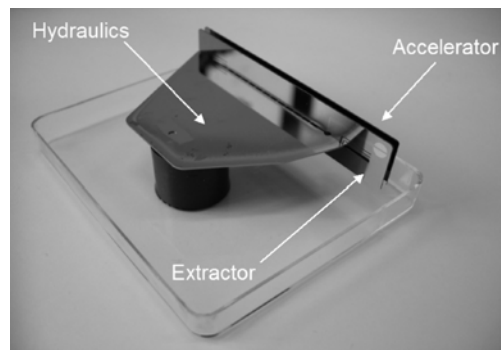


Fig. 1. A linear array of microfabricated electro spray emitters. The device has a system of mesoscaled DRIE-patterned deflection springs to assemble the main body (hydraulics) to the electrodes (extractor and accelerator), in an out-of-plane fashion. The maximum allowed misalignment is set at $60\ \mu\text{m}$ for an electrode with an aperture $300\ \mu\text{m}$ wide, separated $250\ \mu\text{m}$ from the emitter tips.

the minimum feature size (MFS) but still use in-plane feature transfer [3], [4]. A number of techniques have been proposed to give three-dimensionality and/or high aspect ratio to MEMS, including wet/dry etching with some degree of isotropy [5], [6], lattice-oriented etching [7], LIGA (a German acronym for x-ray photolithography, electrodeposition, and molding) [8], SU-8 [9], [10], polymethylmethacrylate [11], and electrochemically welded metallic structures [12].

Also, the range of devices that can be microfabricated would be extended if subsystems of the same device that have incompatible process flows could be built on different substrates, i.e., decoupled, and assembled later. In particular, some device subsystems are incompatible with high temperature, large forces, and/or electric fields because of their thermal budget or change of phase/electrical constraints. In these instances, standard assembly techniques such as fusion bonding [13] and anodic bonding [14] are not viable. Assembly methods that do not include high pressure, temperature, or electric fields have been reported, in particular, a microfabricated velcro [15], and mating convex and concave microfabricated elements [16]. The benefits of process flow decoupling include i) the reduction of parasitic effects between the two pieces of hardware that are joined and/or ii) the implementation of efficient tradeoffs between the device fabrication and its performance [17]. The design decision to decouple the process flows also allows us to optimize the substrate selection for each subsystem.

Another active area of MEMS integration research involves MEMS devices that have subsystems with different characteristic lengths, where these subsystems are intended to be assembled in a specific spatial configuration with adequate precision.

For example, it could be required to input the signal of an optical fiber to a MEMS chip, and precise alignment of the optical fiber axis with respect to the sensing area of the MEMS is required. For this particular example, both silicon and silicon nitride springs have been reported [18], [19].

We present a novel assembly technique that addresses the three-dimensionality of MEMS, the choice to decouple subsystem process flows, and the integration of subsystems that have characteristic lengths of different order of magnitude. The technique involves the use of clusters of mesoscaled passive deflection springs patterned with deep-reactive ion etching (DRIE) and takes advantage of the structural high-performance of single-crystal silicon. The dimensions and specifications of these springs are such that they allow hand assembly of the different substrates in a preestablished spatial relation and precision. We believe that this assembly technique will help expand the range of MEMS that can be implemented. We have demonstrated several MEMS that use a system of deflection springs in their assembly. These MEMS are a linear array of internally fed electro spray emitters (Fig. 1), a linear quadrupole part of a micro gas analyzer (Fig. 2), and a test structure for a planar array of externally fed electro spray emitters [20].

In all three cases, we believe that the introduction of a set of mesoscaled deflection springs simplified the process flows and the packaging/assembly of the devices. The following are brief descriptions of how the specific requirements of these MEMS benefited from the mesoscaled spring system that we propose.

- The electro spray arrays that we developed are intended for space. The working environment includes high vacuum and large temperature differences due to the day/light cycle of an object orbiting around the Earth. Also, these devices could see voltages up to 5000 V [21]. These devices require electrical integrity against ordinary breakdown at high voltage, and robustness against shorting via surface layers of contaminants. Several research teams have pointed out that providing electrodes to dense electro spray emitter arrays is a challenging problem because of the dimensional range (features with different order of magnitude), electrical breakdown requirements, and the high voltage levels that are involved [22], [23]. An ideal electrical insulation should include mesoscale gaps (250 μm to 2 mm) between the electrodes and the emitters, thick dielectric films/dielectric substrates, and minimal physical contact between the electrode and the emitter substrate, far from the emitter area (for practical purposes the emitters then would be hovering right in front of the emitter tips, without physical contact that could eventually produce an electrical short if covered with debris). Materials such as plastics are not desirable for space applications because they outgas, and they have high sputtering yield; this restriction makes unfeasible many of the packaging processes that are available to MEMS. Furthermore, some researchers have reportedly not been successful in using extractor grids as part of the macrosized package of electro spray MEMS arrays [24]. Because of all of the above, we decided to make the MEMS devices with integrated packages and integrate as

many subsystems as possible at the chip level. For an array of electro spray emitters, it is desirable to have good precision during the assembly because we can make the emitter array denser. For the particular case of the linear array that we developed, the maximum misalignment will lead to electrode particle interception is 60 μm . For the particular case of the planar array, the maximum misalignment before particle interception is set at 25 μm . In both cases, any misalignment on the emitter-electrode setup will introduce aberration effects to the emitted stream. In order to minimize the aberration effects, it is important to align as well as possible the electrodes with respect to the emitters, ideally implemented as a self-aligned structure [25], [26]. The design selection of having electrodes supported in a few points with dielectric standoffs is common to many electric propulsion space engines [27]. Also, it is desirable to have a constant separation between the emitter tips and the extractor because the startup voltage of an electro spray engine is dependent on the emitter-to-electrode distance, and we would like to have the emitters activated at the same voltage level while avoiding multicone emission from any spout.

- Linear quadrupoles are devices that filter species based on their specific charge and are often used in mass spectrometry. Depending on the stability region where they operate, linear quadrupoles could require electrode aspect ratios as large as 60 or more to be able to resolve light ions (20 amu or less) with good resolution (1% or better) [28]. The resolution and ion transmission of these devices is greatly influenced by the misalignment in the relative positions of the rods, as well as its taper [29]. Work has been reported on the development of linear quadrupoles that use KOH grooves to support macrofabricated electrode rods [30]. We have implemented a MEMS linear quadrupole that can use electrodes with aspect ratios of 60 or more and diameters down to 500 μm . This quadrupole uses a system of mesoscaled DRIE-patterned springs that allow an alignment precision that we estimate equal to 5 μm or better for the electrodes. The precision of the electrode diameter is also 5 μm .¹ The advantage of this quadrupole concept over the KOH approaches that have been reported is its manual assembly and the fact that the rods can be mounted and dismounted as desired, making the same “spring head” (MEMS structure that has the mesoscaled springs, whose function is to grab, align, and lock the electrode rods) reusable with different aspect ratios to be able to perform under different conditions of pressure, voltages, frequencies, etc.

The following section presents the design considerations for the mesoscaled DRIE-patterned deflection springs. Sections III and IV will focus on the test structure that we developed for the spring system of the linear array of electro spray emitters. This test structure was selected to illustrate the assembly technique because of the extensive modeling and experimental validation we conducted. In Section V, we discuss the alignment precision limits of the assembly technique.

¹The rods were supplied by Small Parts, Miami Lakes, FL.

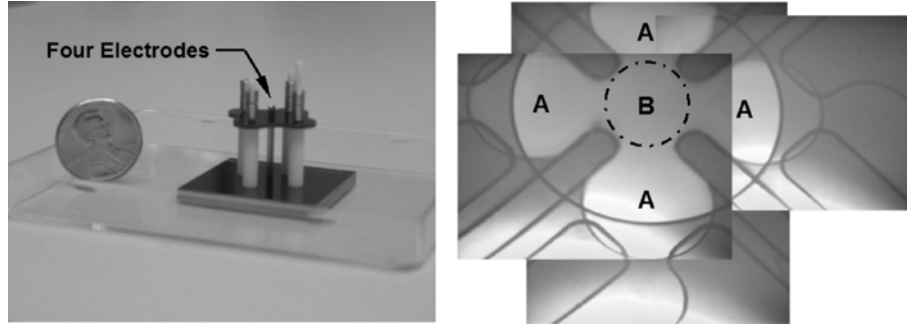


Fig. 2. A linear quadrupole, part of a microfabricated gas analyzer. The device has a system of mesoscaled DRIE-patterned deflection springs that assemble the stainless steel rods. The quadrupole base is integrated with a substrate that has field ionizers. On the left, there is a picture of an assembled quadrupole (quadrupole rod diameter is 0.5 mm). On the right, there is a collage of infrared microscope pictures that show the deflection spring system that was implemented. The quadrupole rods are intended to (A) occupy the four circular cavities (B) surrounding the active area of the quadrupole. The maximum acceptable misalignment is set at $5 \mu\text{m}$ or better.

II. DESIGN CONSIDERATIONS FOR SILICON DRIE-PATTERNED DEFLECTION SPRINGS

The proposed guidelines for this assembly technology are as follows.

- It should be possible to manually assemble the two substrates while preserving good alignment. The alignment requirement is deeply related to the application and the device that implements the spring technology. Good alignment is achieved by taking advantage of the magnitude of the dimensional uncertainty of the microfabrication techniques, in particular contact photolithography and DRIE, compared to the dimensions of the springs.
- The roughness of the surfaces that interact in the assembly should be small enough to prevent the springs from “jamming” at a point different from their final positions. Closed-loop feedback of the assembly operation relies on being able to differentiate when the springs are sliding from when the springs reached their final assembly position by using tactile sense.
- The spring design should incorporate the dimensional variations of the substrates that take part in the assembly, that is, the thickness variation of the springs and the substrates that are clamped by the springs. The spring elastic performance should provide for activation at a range of displacements compatible to this substrate variation.
- The displacement springs are slender, and the spring deformation is smaller than any of their characteristic dimensions (width, height, and length). As a rule of thumb, the length-to-height ratio should be at least ten and the displacement should be at most equal to the height value [31].
- The frictional force that the two pieces produce when sliding is used as feedback for the assembly. We suggest keeping the clamping force on the order of 1 N in order to have friction forces on the order of a fraction of a newton. This frictional force level is large enough to be discernible from noise sources by the tactile sense of human hands and from the final position of the assembly (the springs get jammed).

The material of the mesoscaled deflection springs is silicon. Silicon can be modeled assuming an isotropic, elastic behavior with a Young’s modulus equal to about 145.5 GPa [31]. It is

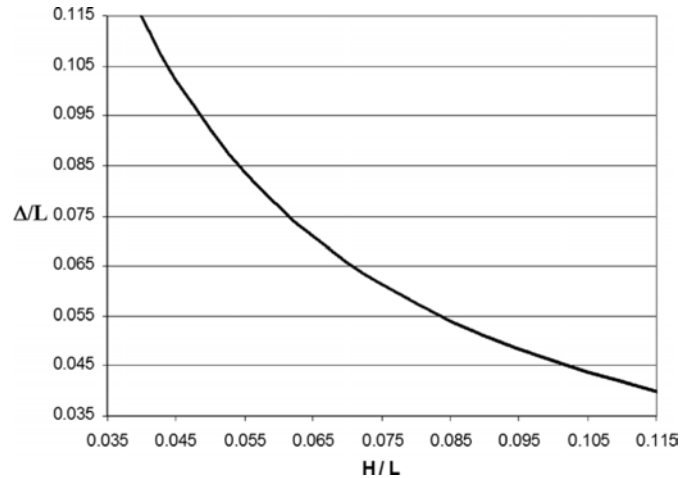


Fig. 3. Δ/L versus H/L for silicon. The dimensionless parameters can be at either axis because they are inversely proportional. As a rule of thumb, both dimensionless parameters should be smaller than 0.1 in order to satisfy the slender body/small deflection requirements of the model.

stated in the literature that this approximation shows good agreement with modeling of silicon as a cubic lattice [32]. The high aspect ratio and small deflection of the mesoscaled springs allow us to model their elastic behavior using the beam equation [33]

$$\frac{d^2 u_y}{dy^2} = -\frac{M}{E \cdot I} \quad (1)$$

where u_y is the displacement perpendicular to the beam neutral fiber, y is a variable along this direction, E is Young’s modulus, M is the bending moment, and I is the area moment of the beam. The springs are modeled as a cantilever beam of uniform cross-section with a point load F applied at the beam tip, separated a distance L from the fully constrained end. Each spring is assumed to be decoupled from the influence of any of the other springs. The maximum deflection Δ (the beam tip) is then

$$\Delta = \frac{F \cdot L^3}{3 \cdot E \cdot I} \quad (2)$$

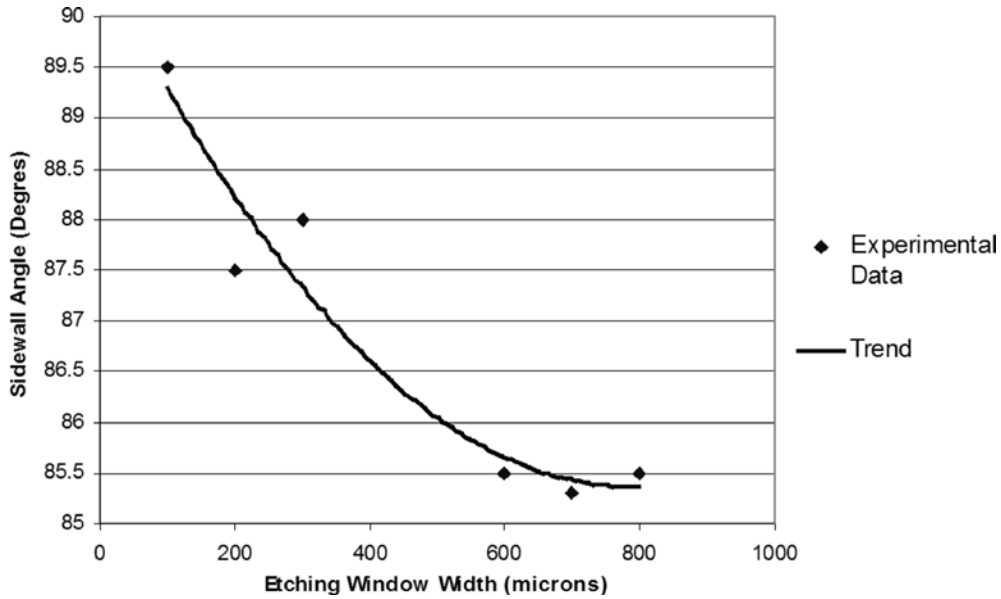


Fig. 4. Etching sidewall angle versus etching window width for DRIE-patterned features that use oxide as etching mask. A plasma confinement effect takes place when the etching window is narrow enough ($< 100 \mu\text{m}$), enabling us to pattern straight walls.

For a beam with rectangular cross-section, the relationship between applied force and maximum deflection is

$$F = \frac{\Delta \cdot E \cdot b}{4} \left[\frac{H}{L} \right]^3 \quad (3)$$

where b is the beam width and H is the beam height. On the other hand, the relationship between the maximum stress σ_m and the maximum deflection Δ for the same beam and load situation is

$$\sigma_m = \frac{3}{2} \cdot E \cdot \frac{\Delta \cdot H}{L^2}. \quad (4)$$

The last two equations can be used to design the deflection springs. The spring design problem is underconstrained; therefore, there is no unique solution for (3) and (4) for the actual beam dimensions. As a matter of fact, there are a number of spring geometries that can achieve the same criteria (deflection, stress levels below a certain value, buckling resistance, etc.), which encompass substantial variations in the spring length, width, and height.

The criterion for stress failure in a brittle material is the maximum principal stress [34]. Ceramics withstand far better compressive loads than tensile loads, reinforcing the fact that the failure criterion is the existence of tensile stresses larger than a given threshold value; also, ceramics show a probabilistic behavior. The allowed stress level is proportional to the processing-induced flaw population, in particular the roughness present in sharp changes of topography [35]. For a DRIE-patterned part whose roughness was smoothed, the maximum allowed tensile stress is around 1 GPa, with a failure probability of 0.5% and a confidence of 95% [32], [35].

The dimensionless expression $D \cdot H / L^2$ [see (4)] has an upper bound for a given material. In the case of silicon, this value

is 4.6×10^{-3} . Fig. 3 shows the relationship between Δ/L and H/L using this upper bound value.

The spring patterning should have sidewalls as straight as possible to dimensionally control the spring geometries. This paper reports the implementation of this assembly technique using DRIE-patterned springs. DRIE has a dependence of the sidewall slope with respect to the etching window width for a given set of plasma conditions.

Fig. 4 summarizes our experimental findings on this regard, using a particular recipe that the Microsystems Technologies Laboratories, Massachusetts Institute of Technology, has developed. The experimental data suggest that for DRIE patterning using oxide etching masks, etching windows smaller than $100 \mu\text{m}$ give sidewall slopes to first order equal to 90° . However, the concept of using mesoscaled springs could be extended to other substrate materials and spring patterning techniques such as laser etching.

There is a third criterion to take into account when designing the mesoscaled springs: during the assembly, the springs should be in tension to avoid the possibility of buckling. In the event of a need to disassemble, or the case of an assembly procedure that requires back-and-forth sliding, it should be possible to compress the springs. The model for buckling that most closely matches the real situation is when one end is totally constrained while the other end is just restricted in displacement in the direction of the deflection w , as shown in Fig. 5.

For this buckling mode F_p , the maximum compressive force before buckling is expressed by [33]

$$F_p = \frac{\pi^2}{6} \cdot E \cdot \frac{b \cdot H^3}{L^2}. \quad (5)$$

The compressive load acting on one of these mesoscaled spring is, to first order, due to the friction produced by the applied force F (the spring force acts as the normal force that generates the frictional load), the ratio between the two

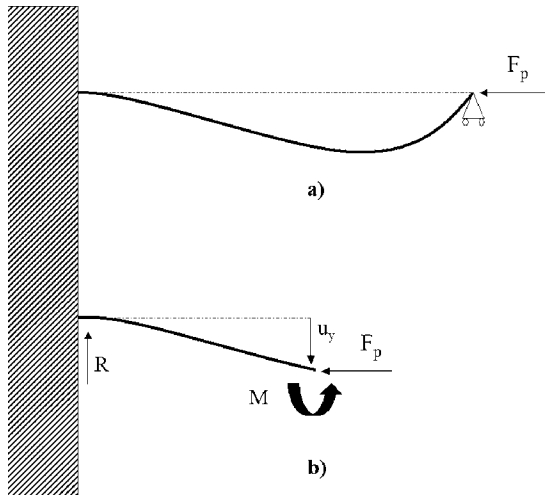


Fig. 5. Schematic of a beam under buckling conditions similar to the ones faced by the spring system when (a) dismantling and (b) free body diagram of the setup. R is the shear force at the fully constrained end and F_p is the compression force acting on the beam.

forces must be larger than the static friction coefficient μ_s to be buckling-safe. The ratio between the two forces turns out to be a geometrical criterion between the beam length and the maximum deflection

$$F_p \geq F \cdot \mu_s \Rightarrow \frac{2 \cdot \pi^2}{3} \cdot \frac{L}{\Delta} \geq \mu_s. \quad (6)$$

Static friction coefficients are smaller than one [36]. Therefore, the criterion imposed by (6) is already satisfied for a spring designed with the beam equation. Finally, it is important to emphasize that DRIE-patterned structures increase their structural performance if they receive a smoothening posttreatment, in particular with an SF_6 plasma [32]. In the case of out-of-plane assemblies, the use of double-side-polished wafers provides very smooth surfaces to the spring tips for assembly interaction.

The springs should have a smooth geometry in order to avoid stress concentrators. The spring geometry should also take into consideration some inlet features, that is, a set of shapes that facilitates the initial approach between the two parts to make contact.

III. DESIGN EXAMPLE: A SPRING SYSTEM TO ASSEMBLE MICROFABRICATED ELECTRODES TO AN ELECTROSPRAY ARRAY

Fig. 6 shows one of the test structures implemented to analyze the spring assembly system of the electrospay linear array that we developed [21].

The design of this particular linear array requires an out-of-plane substrate assembly between two microfabricated electrodes and the device hydraulics with precision equal to $60 \mu\text{m}$ or better, while providing $250 \mu\text{m}$ of separation between the emitter tips and the closest electrode (extractor). Also, the electrode-emitter setup should not implement a closed geometry. That is, there should be minimal physical contact between the electrodes and the hydraulics substrate, and the points of contact between the electrodes and the hydraulics substrate should be far from the emitters.

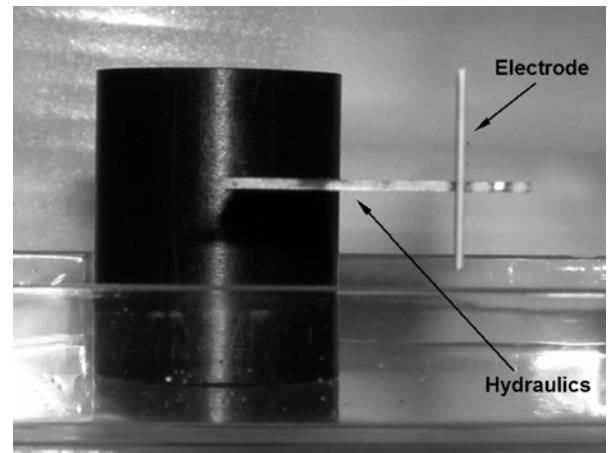


Fig. 6. Picture of an assembled test structure of the spring system a linear electrospay array. The test structure is seen from the side. The perpendicularity of the assembly is clear from this picture.

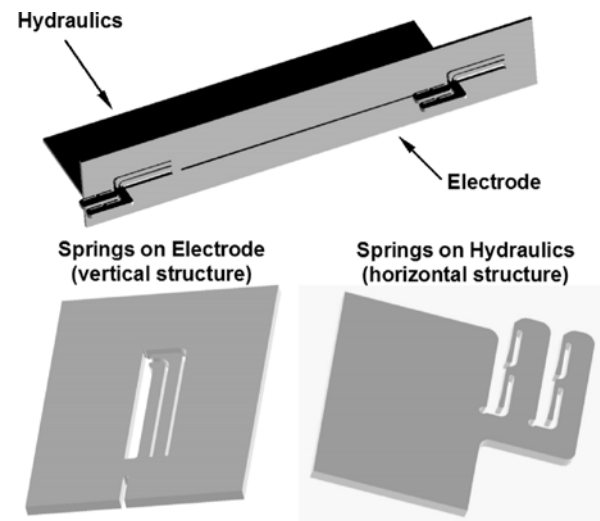


Fig. 7. (Top) 3-D model of the out-of-plane test structure that was implemented and (bottom) zoom of the two kinds of spring clusters. In the electrospay linear array, the spring cluster on the lower left is patterned in the electrode substrates, while the spring cluster on the lower right is patterned in the hydraulics wafer stack.

Fig. 7 shows a three-dimensional (3-D) model of the test structure with closeup images of the two types of spring clusters used. One set of spring clusters is patterned into the hydraulics wafer stack, while the second set of spring clusters is patterned into the electrode substrates. Table I summarizes the dimensions of the two types of springs that are in the test structure.

The dimensions of the springs reflect the required performance under the constraint of the available space on the mask. With the exception of the substrate thickness (the beam width), the test structure has the same geometry and dimensions that we eventually implemented in the linear array. The wafer thickness difference has no effect on the validation of the spring system because the spring width does not affect the stress levels (planar stress state is assumed). The spring width only changes the force that the spring tips exert for a given deflection. This force scales linearly with the spring width. The displacement value for the main body test structure was set at $50 \mu\text{m}$ to be one order of

TABLE I
DIMENSIONS OF THE SPRINGS IMPLEMENTED IN THE OUT-OF-PLANE ASSEMBLY TEST STRUCTURE. THE FREE-LENGTH IS DEFINED AS THE DISTANCE FROM THE SPRING TIP TO THE POINT OF MAXIMUM TENSILE STRESS

Feature	Free Length (μm)	Height (μm)	Width (μm)	Nominal Deflection (μm)
Main Body test structure substrate	2000	225	600	50
Electrode Test Structure Substrate	8100	750	600	100

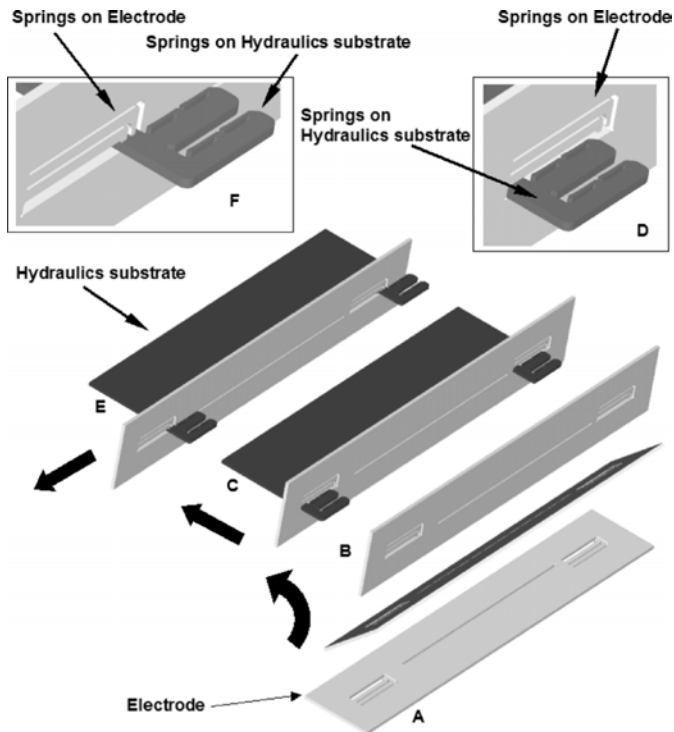


Fig. 8. 3-D model to illustrate the assembly of the test structure. The electrode substrate (A) is first rotated 90° (B), so it can face perpendicularly the main body. Then, the electrode substrate is pushed up to make contact with the main body substrate (C). This last operation is made making sure that the spring clusters of the main substrate pass through the cavities in front of the electrode spring clusters (D). Finally, the electrode is pushed to one side to make the springs of both substrates activate (E), until the edges of the two substrates make physical contact (F). In this assembly procedure the springs are in tension. The arrows indicate direction of movement of the electrode substrate with respect to the main body substrate.

magnitude above the wafer thickness uncertainty ($\pm 5 \mu\text{m}$). The displacement value for the electrode test structure was set at $100 \mu\text{m}$ because we had more room in the electrode mask, allowing us to pattern larger spring geometries.

A. Fabrication

The process flow for the out-of-plane substrate assembly test structure starts with double-side-polished silicon wafers, $600 \pm 5 \mu\text{m}$ thick. Then, a layer of plasma-enhanced chemical vapor deposited (PECVD) oxide $11.5 \mu\text{m}$ thick is deposited on both surfaces of the wafer (one film will be used as etching mask, while the other film is used as etch stop and for wafer bow compensation). The oxide thickness was determined with due consideration for the etching selectivity of the DRIE and the electrical insulation required for the electro spray array. After the oxide films were deposited, they were annealed at 1050°C in a

nitrogen atmosphere for 1 h, in order to improve their quality. After the annealing, $8 \mu\text{m}$ of photoresist AZ 4620 was spun on one of the sides, and the spring clusters were defined using contact photolithography. Then, the spring cluster patterns were transferred to the silicon oxide film using RIE in an Applied Materials Etcher 5300. The thickness of the photoresist was selected based on the selectivity of the RIE recipe that we used to pattern the oxide. After the oxide film is patterned, the silicon substrate is mounted to a quartz handle wafer using photoresist. The silicon wafer is then etched all the way through using a Surface Technologies System DRIE tool. After the DRIE patterning, the roughness of the structures is smoothed using an SF_6 -based plasma. Finally, the test substrates are released from the handler wafer using acetone. The test structure substrates are cleaned, dipped in HF 49% pure to strip the oxide films, and then hand assembled using a pair of tweezers. The substrates were first brought into close proximity and then slid until the springs reach the end of the sliding paths. Fig. 8 shows a 3-D model of the way the test structure substrates are assembled.

IV. RESULTS

A. Comparisons of Design Equations With Simulations

Equations (3) and (4) constitute a simple reduced-order model of the structural performance of the mesoscaled DRIE-patterned springs. In order to validate the usefulness of the reduced-order model, 3-D finite-element simulations of the spring clusters were conducted using the commercial software Ansys. The mesh was refined until the change in the nodal solution of the stress field was smaller than 5%. The geometry and dimensions of the spring clusters were mapped as closely as possible to the real spring layouts using the commercial software AutoCAD. The wafer thickness of the substrates used in these models is $600 \mu\text{m}$. We encountered stiffness problems with the Ansys simulations when we tried to upload the geometry with dimensions declared using the international system. We found that if we used as unit of length a micrometer, the stiffness problems disappeared. If the mass and time units are kept unchanged, then this change in units makes the stress unit be equal to 1 MPa. Therefore, all results from the software package will show stresses in MPa and displacements in micrometers. Also, the displacement field in the graphical results has been exaggerated to better illustrate it. The simulations had four goals.

- 1) To demonstrate that each spring acts independent of the stress state of the other springs. This was verified visually by looking at the solutions of the stress and displacement fields when a portion of the springs is activated. As an example, Fig. 9 shows the stress field and deflection of

the set of springs that are patterned on the hydraulic substrate that are intended to assemble the closer electrode to the emitter tips. Nonzero stress levels and displacements are restricted to only the spring bodies that were activated. However, Fig. 9 also indicates that the material that is intended to constrain the rotation and the displacement of the spring root has a nonzero stress level. Therefore, the boundary value at the root of the springs is not a true fully constrained joint. Despite this, the maximum stress occurs at the point of maximum bending moment, and it occurs at about the spring free-length from the spring tip.

- 2) To determine the maximum principal tensile stress that is present at the spring root of both spring geometries when the deflection of the spring tips is the nominal deflection value. The finite-element simulations used the spring tip deflection as nonzero boundary value, while the farthest nodes of the mesh were constrained both in displacement and rotation. In this scheme, the forces at the spring tips are part of the nodal solution. A summary of the simulation findings is in Table II. The results demonstrate good agreement between the reduced-order model and the finite-element simulations. There is no monotonic tendency of the reduced-order model to either underestimate or overestimate the stress level.
- 3) To determine the force that has to be applied to the spring tips of both spring geometries to produce a deflection equal to the nominal deflection value. In order to establish this force, we conducted a series of simulations where the nonzero boundary values were the forces at the spring tips (the farthest nodes were still constrained both in displacement and rotation). These forces were augmented until the displacement at the spring tips reached the nominal displacement value. A summary of the simulation findings is in Table II. As in the case of the stress-level simulations, the displacement results demonstrate good agreement between the reduced-order model and the finite-element simulations. However, the results suggest that the reduced-order model tends to overestimate the clamping force. We think that this discrepancy comes from the fact that, in reality, the spring root is not fully constrained because the spring root is connected to a piece of material with finite stiffness, thus giving to the structure freedom to rotate (there is a tradeoff between induced stress and the deflection/rotation at the boundary of a beam), thus making the spring less stiff than what the model predicts.
- 4) To determine whether or not the proposed assembly feedback is feasible. The proposed assembly technique relies on a large contrast between the friction force and the reaction force that the springs produce when pushed while they are at their final positions. For two smooth surfaces (the smoothed DRIE surface and the unperturbed silicon surface), the friction force is at most of the magnitude of the clamping force. A series of simulations were conducted to determine what was the maximum force that either structure could withstand before failure. For springs on the hydraulics, the failure mode would be to create enough stress at the root of the structure that holds the spring clusters (Fig. 10). Using finite-element simulations, we determined

this value to be equal to 120 N for the inner spring set and 42 N for the outer spring set. The same considerations were pondered for the springs on the electrodes. In this case, the structural failure would occur at the frame that surrounds the spring clusters. For the electrode spring cluster, the maximum force at the point of failure is 128 N. In all cases, the force that causes structural failure is at least an order of magnitude larger than the frictional force, consistent with the assumption that the two forces can be distinguished when assembling the two substrates.

B. Wafer Assembly

The assembly of the test structure was readily carried out using a pair of tweezers, using as feedback the frictional force produced when the two substrates are brought into contact. Fig. 6 shows one of the test structures assembled using the procedure described in Fig. 8. Fig. 11 shows two scanning electron microscope (SEM) pictures of one of the assembly joints, looking at the structure from both sides. Fig. 12 shows a closeup view of the electrode root area and Fig. 13 shows the interface between the electrode frame and one of the hydraulic spring cluster roots.

Several key issues can be identified in this set of pictures.

- The springs are deflected, i.e., there is zero-gap between the spring tips and the unperturbed reference surfaces. Therefore, the pieces are making physical contact.
- The physical contact between the springs and the clamped substrates is made exclusively at the spring tips. Given the sidewall taper, this contact is made at a point instead of a line. This does not represent a problem because we observe experimentally that the springs make a stiff assembly.
- The assembly is made with two assembly joints. Each joint is controlled with at least nine points of contact, spanning the three degrees of freedom. Eight points of contact come from the springs and control two axes. The presence of a well-defined stopping point at the spring cluster roots allows us to control the third degree of freedom (DOF) not directly controlled by the spring clusters, and this adds up to two additional points of contact to the assembly. The number of points of contact is enough to assure the control of the rotations and axial displacements.
- It is always possible to slide the electrodes down to the spring cluster roots without causing structural failure. In a few cases, we found an indentation produced at the point of contact between the two substrates, along the degree of freedom that is not controlled by the spring clusters (Fig. 13). This fissure is related to the stress concentration at the substrate edge due to the formation of an etching taper. Based on our testing experience, and the results from the finite-element simulations, we concluded that the presence of this crack does not substantially change the stress level of the springs and thus, the safety factor of the assembly is not sensibly diminished.
- There is no evidence of cracking in the spring structures. Given the fact that silicon is a fragile material, the stress levels of the springs are below failure values.
- Several test structures were assembled, and the test structure never failed during assembly. This validates the proposal of hand assembly without any other auxiliary equip-

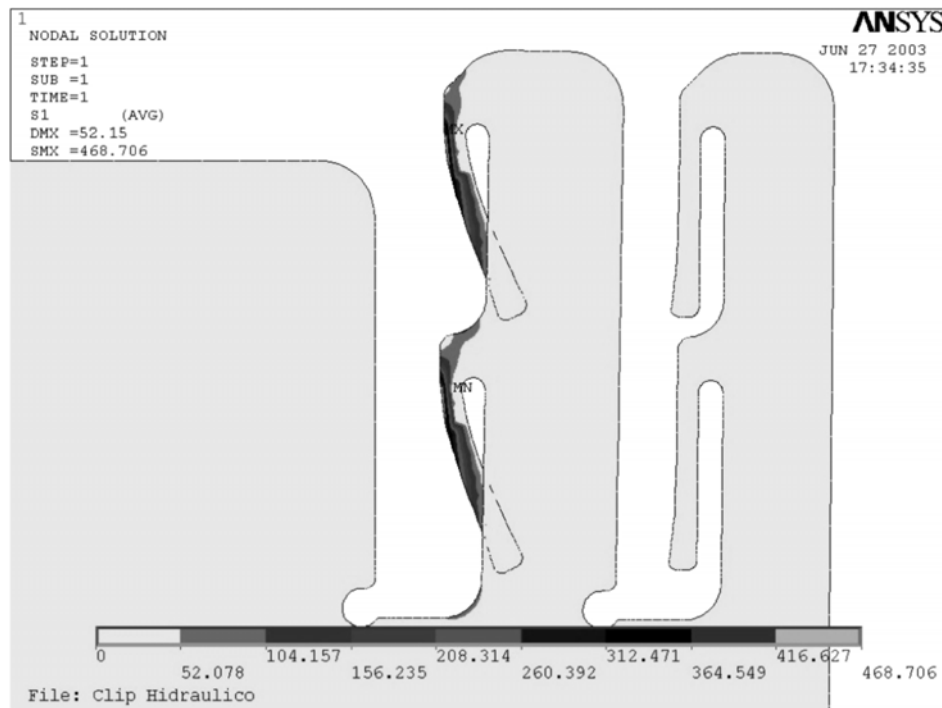


Fig. 9. Graphical result of the finite-element analysis of the spring cluster carved on a main body test structure substrate. In this particular simulation, only the internal springs are activated. The deflection at the emitter tip is 50μ and the maximum tensile stress is 468.7 MPa.

ment beyond a pair of tweezers (no sliding guides, other than the actual spring cluster roots, are needed).

- Experimentally, it was found that the stiffness of the joint is increased if the force exerted by the springs is increased; this suggests setting larger nominal spring deflections but keeping in mind that the friction forces should be distinguishable from the force produced by final position of the assembly.

1) *Metrology of the Assembly:* After demonstrating the feasibility of the proposed assembly technique, we conducted experimental measurements of the relative position of the electrode with respect to the hydraulic substrate to estimate the misalignment. We processed six batches of devices, obtaining 12 devices out of them that were subject to the battery of measurement procedures that are describes in this section.

Measuring the substrates before assembly (in-plane metrology) became the first test conducted on the assembly. In doing this, we checked key layout features to the corresponding test structure values. Using an optical microscope, the dimensions of the key features of the spring structures were within $4 \mu\text{m}$ from the corresponding dimensions on the optical mask, when measuring the side that directly received the photolithographic process. These values are consistent to what we were expecting from contact photolithography and the RIE of the oxide. We also die-sawed several devices to determine the taper dependence on etching window. The results are summarized in Fig. 4. In all cases the taper is negative, which means that the cavity becomes wider the deeper it is. The conclusion from the experimental characterization of the taper is that etching windows smaller than $100 \mu\text{m}$ should give etched sidewalls that are to first order perpendicular.

Next, we measured the nonperpendicularity of the two substrates (Fig. 14). To determine the misalignment of the

assembly, we measured the angle between the electrodes and the hydraulic substrate using high-resolution digital pictures of several assembled test structures and AutoCAD. A nonperpendicular assembly can lead a nonuniform field around the emitter tip for electro spray arrays, causing nonaxial emission of propellant. The trajectory of the emitted particles is tilted more when the charged particles get closer to the electrode. The emitted particles make a fan with a divergence angle due to the Coulomb repulsion of the particles. The semiangle of the emitted fan is estimated at 20° for formamide [21]. For an electrode $300 \mu\text{m}$ wide separated $250 \mu\text{m}$ from the emitter tips, the maximum tilting angle before particle interception is then about 10° . Based on the data that we took, we concluded that the average angle between the electrodes and the main substrate is 89.86° with standard deviation equal to 0.45° . This result demonstrates the feasibility to perpendicularly assemble two substrates with mesoscaled DRIE springs.

The displacement misalignments were also estimated for the 12 assembled devices using a Hawk three-axis optical microscope from Vision Engineering, with a measurement uncertainty of $0.5 \mu\text{m}$. It is important to keep in mind that measurement of misalignment of the assembly is difficult because the two substrates are on different planes, imposing some experimental constraints. We will explain how we carried out the measurements in each direction. Before introducing the data, we would also like to explain how a certain misalignment level in a particular direction affects the performance of the device. The proposed misalignment definitions are referenced to a linear electro spray array that places the emitters at the interface of a two-wafer stack.

There are two independent sources of misalignment that influence the performance of the device. One source of misalignment is the error introduced by the assembly; the other source is

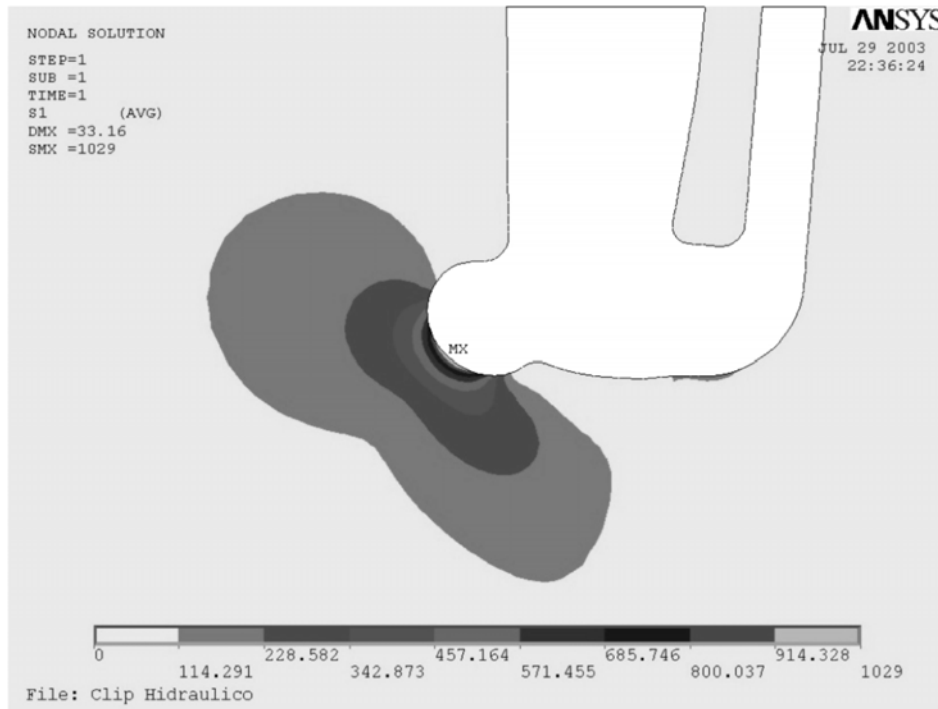


Fig. 10. Solution of the stress field main body test structure when an internal electrode is pushed with a downward force of 120 N.

TABLE II
BENCHMARKING OF THE REDUCED-ORDER MODEL WITH FINITE-ELEMENT SIMULATIONS. THE VARIATION IS DEFINED AS DIFFERENCE OF THE REDUCED-ORDER VALUE WITH RESPECT TO THE FINITE-ELEMENT VALUE

Quantity	Finite Element Result	Reduced-order Model	Variation
Max. Tensile Stress, Main Body Test Structure, Nominal Deflection (50 μm)	450.2 MPa	613.8 MPa	26.7%
Max. Tensile Stress, Electrode Test Structure, Nominal Deflection (100 μm)	313.9 MPa	234.8 MPa	33.7%
Force at Spring Tip, Main Body Test Structure, to achieve Nominal Deflection	1.29 N	1.55	17.0%
Force at tip of Spring, Electrode Test Structure, to Achieve Nominal deflection	1.17 N	1.58	26.0%

the error due to the fabrication of the device, in particular by the taper of the DRIE etching. It is clear that the shift in position of the emitters because of the fabrication taper is not caused by the assembly, but it influences the goal of having a set of emitters uniformly separated from an electrode a given distance (Fig. 15). In the test structure, the midpoint of the emitter is not a specific feature; therefore, we estimated its position based on the assembly and the assumption that the DRIE taper is a straight line through the whole substrate thickness. The following are the descriptions of the misalignment on each axial DOF of the test structure assembly.

- ΔZ : The z -axis is defined as the direction perpendicular to the plane defined by the electrode (Fig. 16). A misalignment in this direction will produce a change in the emitter starting voltage because it has a dependence of the form [21]

$$V_{\text{start}} = \sqrt{\frac{\gamma \cdot L_{c,o}}{\epsilon_o}} \ln \left[\frac{4G}{\sqrt{L_c \cdot L_{c,o}}} \right] \quad (7)$$

where L_c is the inner diameter of the emitter, $L_{c,o}$ is the outer diameter of the emitter, G is the emitter-to-electrode separation, ϵ_o is the electrical permittivity of free space, γ is the surface tension of the propellant that is used by the electro spray array, and $4G > (L_c \cdot L_{c,o})^{0.5}$. The effect of an offset in the z -axis in the startup voltage is mild because of the logarithmic dependence of the startup voltage with respect to the emitter-to-electrode separation. Also, the shift in startup voltage is global; thus it does not perturb the performance of the device as an array. When we designed the electro spray array, we made a tradeoff between small startup voltage (~ 1000 V) and moderate sensitivity to emitter-to-electrode separation offset. It is important to point out that a variation in the startup voltage can be addressed by the power supply, provided it does not lead to electrical breakdown. For the particular device, this value is set at 2500 V if we assume good vacuum levels.

- ΔX : The x -axis is defined as the direction in the plane defined by the electrode test structure that is parallel to any

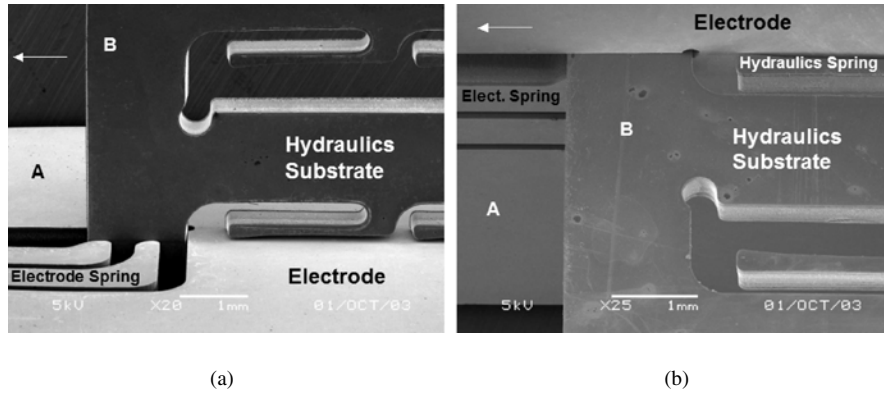


Fig. 11. SEM pictures showing the activation of a spring set that compose an assembly joint: (a) front view of the four springs and (b) closeup back view of a spring tip. The electrode test structure (A) is completely slid down to make physical contact with the corresponding root of spring cluster carved on the main body test structure (B). The arrow shows the relative sliding direction of the electrode respect to the engine hydraulics. In (b) there is visible change in shape in the deflected spring (above) compared to the spring that has not been activated (below).

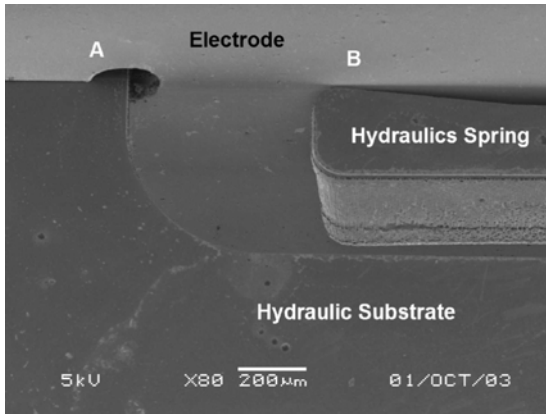


Fig. 12. SEM picture of an electrode spring cluster root and the deflected tip of a spring from the corresponding a main body spring cluster. Looking at the root notch (A), one can see a zero gap between the two substrates at the electrode spring cluster root in the two in-plane independent directions. There is physical contact between the spring tips and the clamped substrate just at the spring tip (B).

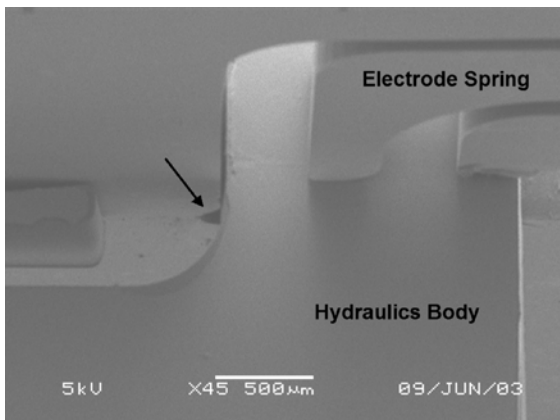


Fig. 13. SEM picture showing three springheads of the same assembly joint deflected and a defect caused by the assembly procedure. A small superficial crack is present at the point of contact of the two substrates, in the direction of the degree of freedom that is not directly controlled by the spring clusters (arrow). The crack is believed to be produced by stress concentration at the substrate wedges when brought into contact.

line that joins two emitter centers (Fig. 17). For an electrode that provides an individual hole for each emitter, a

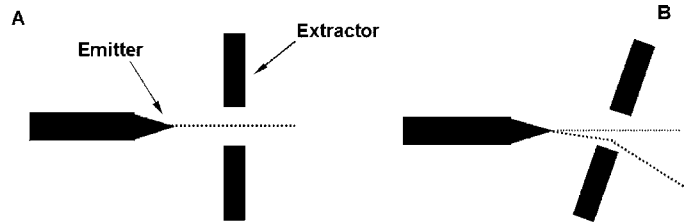


Fig. 14. Effects due to assembly nonperpendicularity. Ideally, the assembly is perpendicular, so the emitter is surrounded by a uniform field, producing axial emission (A). If the assembly is tilted, there are regions of the emitter that are closer to the extractor, having a higher local electric field. This field enhancement will produce the emitters to fire nonaxially (B). The nonaxial trajectory of the emitted particles will be augmented by the effect of the electrode, as they drift through.

misalignment in the x -axis produces off-axis emission and aberration of the electric lens. The electrode is a slot to make the assembly insensitive, to first order, to misalignments in the x -axis.

- ΔY : The y -axis is defined as the direction in the plane defined by the electrode test structure that is perpendicular to any line that joins two emitter centers (Fig. 18). For any electrode (individual holes, slot), a misalignment in the y -axis produces off-axis emission and aberration of the electric lens. The maximum misalignment for a $300\text{-}\mu\text{m}$ -wide electrode, separated $250\ \mu\text{m}$ from the emitter tip, is set at $60\ \mu\text{m}$. Any larger misalignment will lead to particle interception by the electrode.

It is clear from the previous definitions that the most troublesome of the emitter misalignments is ΔY . Fortunately, measurement of the ΔY misalignment is straightforward metrology. However, we also took measurements of ΔX and ΔZ to obtain a complete picture the performance of the assembly technique. The following is a description of the way we conducted the measurements, along with the data we obtained. In all measurements, we optically verified beforehand that the springs were deflected and are occupying their final positions.

- ΔZ : Fig. 19 describes the testing procedure determining the misalignment along the z -axis. We used two tilt angles on each side of the assembly to make sure we did not have systematic measurement errors due to tilting the assembly. We measured the assembly looking at the top and

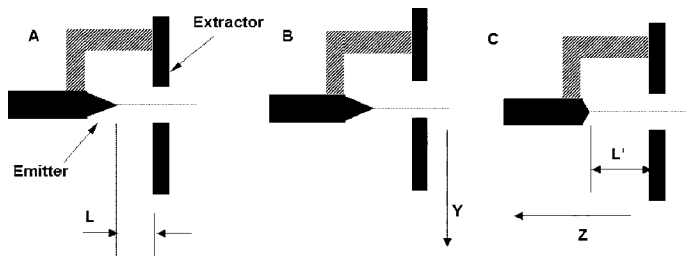


Fig. 15. Assembly offset versus fabrication offset. The goal is to fabricate an array of emitters that are uniformly spaced from some electrode a distance L , with the emitter tips centered with respect to the middle of the electrode aperture (A). One possible departure from ideality is to have the electrode and the emitters shifted because of the electrode-to-emitter assembly (B, Y -direction, the electrode slot is shifted with respect to the emitter tips). Another possibility is to have the setup shifted because of fabrication nonidealities of the emitters or electrode (C, Z -direction, the emitter are blunt due to fabrication issues, setting a different emitter-to-electrode separation L').

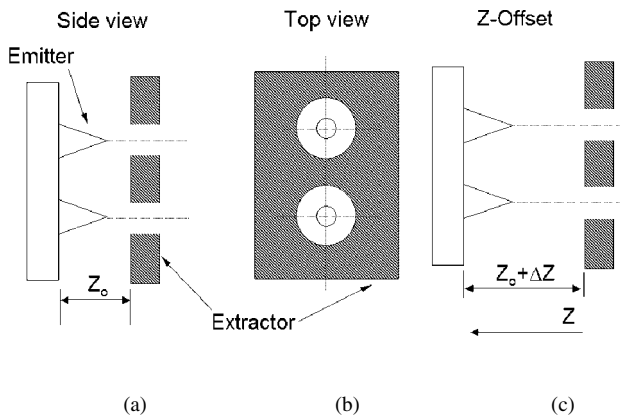


Fig. 16. ΔZ offset. The schematic shows a two-emitter system. (a) and (b) The side view and top view of an aligned system. (c) A misalignment on the z -axis. The z -axis is defined as the direction perpendicular to the electrode plane. An offset in this direction introduces a change in the emitter array startup voltage.

the bottom surfaces. If we assume that the assembly is perpendicular, the two sets of measurements (front side, back side) should tell us the misalignment at the midpoint of the substrate. The misalignment in the z -direction has three sources.

- We estimate that the misalignment due to the assembly is smaller than $1 \mu\text{m}$ because there was always a zero-gap between the electrode and the main body and because of the measured electrode-to-main body relative angle.
- The offset due to patterning undercut ΔZ_1 is estimated at $13.25 \mu\text{m}$.
- The average offset due to emitter DRIE tilting $\Delta Z_2/2$ is estimated at $22.5 \mu\text{m}$.

Therefore, the average total ΔZ is estimated at $38.75 \mu\text{m}$.

- ΔX : Fig. 20 describes the testing procedure for determining the misalignment in the x -axis. The average offset between midpoints of the substrates due to the taper ($\Delta X_1/2$) was estimated at $37.31 \mu\text{m}$.
- ΔY : Fig. 21 describes the testing procedure for determining the misalignment in the y -axis. The average offset between midpoints of the electrode and the hydraulic substrates ($L_1/2 - [L_2 + w/2]$) was estimated at $16.34 \mu\text{m}$.

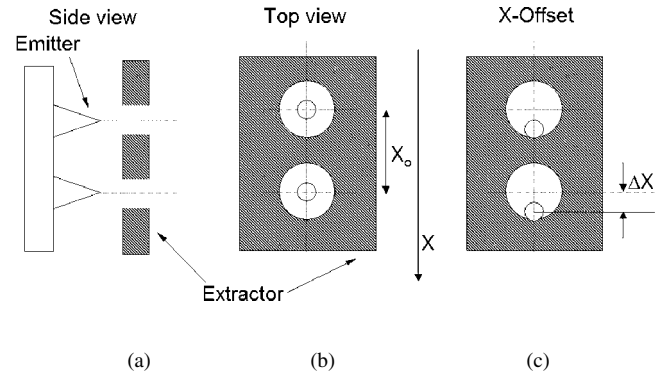


Fig. 17. ΔX offset. The schematic shows a two-emitter system. (a) and (b) The side view and top view of an aligned system. (c) A misalignment on the x -axis. The x -axis is defined as the direction in the plane defined by the electrode that is parallel to any line that connects two emitter tips. An offset in this direction introduces nonsymmetry to the emitter/electrode setup unless the electrode is a continuous slot. This nonsymmetry produces aberration effects and off-axis emission.

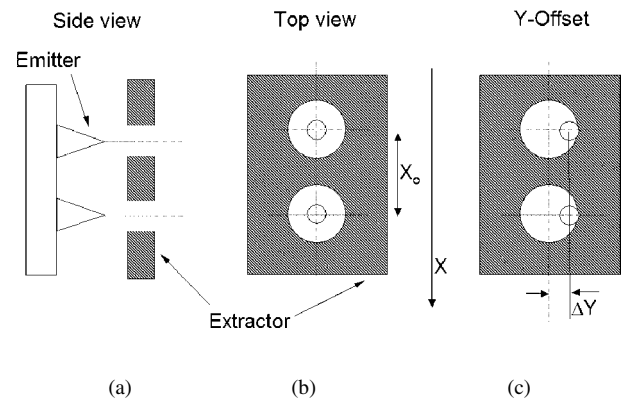


Fig. 18. ΔY offset. The schematic shows a two-emitter system. (a) and (b) The side view and top view of an aligned system. (c) A misalignment on the y -axis. The y -axis is defined as the direction in the plane defined by the electrode that is perpendicular to any line that connects two emitter tips. An offset in this direction introduces nonsymmetry to the emitter/electrode setup. This nonsymmetry produces aberration effects and off-axis emission.

V. DISCUSSION

A. Sources of Misalignment

We believe that the following are the main sources of dimensional variation that could influence the assembly accuracy of the test structure.

- **DRIE roughness.** DRIE produces a substantial amount of roughness compared to other shallower plasma etching treatments. DRIE produces a bite-like pattern at the etched surface because of the cycled nature of the process (passivation/nonpassivation) and the use of SF_6 as etching species. However, the experimental evidence that we obtained suggests that the roughness of DRIE is better described as striations parallel to the etch direction with some characteristic wavelength. Depending on the actual parameters of the etching recipe, the characteristic in-plane wavelength and depth of the roughness are set. We found that the upper bound for the striation depth is about $1 \mu\text{m}$.

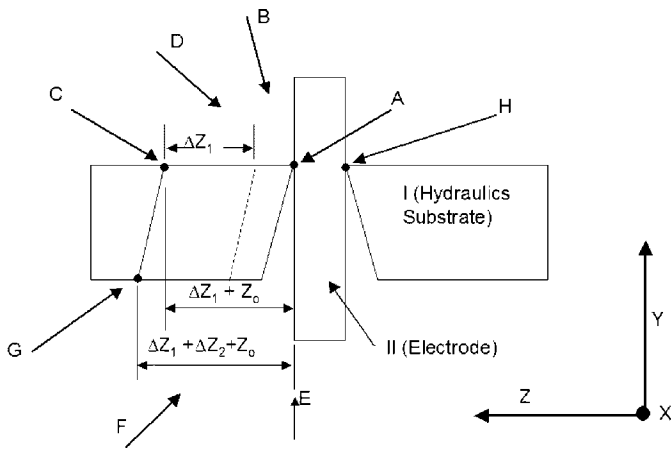


Fig. 19. ΔZ measurement. The assembled test structure brings together the hydraulics substrate (I) and the electrode (II). The assembled structure was measured using a three-axis microscope with resolution of $0.5 \mu\text{m}$. First, the optics are set looking at the top of the device. The testing assembly was then tilted 5° (B), and the interface between the two pieces (A) was aligned to one of the axes of the microscope stage. Then, a measurement of the distance between the interface line and the top of the emitter decoys (C) was carried out. The measurement was repeated with an inclination of 45° (D). In both cases, a projection of the measurement on the plane defined by the main body top surface was conducted. The mismatch between the measurement and the layout values is ΔZ_1 , a value we believe is mainly related to undercut of the layout because of the DRIE patterning. The same measurements were conducted on the backside, with device inclinations equal to 0° (E) and 45° (F). The 0° inclination was used because, if we look at the interface from the backside, the interface (A) is inside a trench. In this case, the edge of the electrode substrate was used as reference line for the misalignment. If the interface is looked at 45° from the backside, the interface is not a line but two points at both ends of the trench. The distance between (A) and the bottom of the array of decoy emitters (G) was measured. The mismatch between the measurement and the value from the layout includes both the undercut offset (ΔZ_1) and the offset due to the DRIE taper (ΔZ_2). The interface between the two substrates (A) serves as pivot for the relative rotation between the two substrates.

- **DRIE taper.** The DRIE etching taper is highly dependent on the actual etching recipe that was used. MIT's Microfabrication Technologies Laboratory has developed a series of recipes that achieve good uniformity and steep etching taper, recipes that we used to fabricate the assembly test structure. We have found that the etching taper is sensitive to the etching window width. An experimental plot of the etching taper versus etching is shown in Fig. 4.
- **RIE taper (etching mask).** The plasma etching recipes that were implemented in a high-density plasma etcher Applied Materials 5300 produced a sidewall of about 80° , even for the thick silicon oxide layers that we used in the process flow of the assembly test structure. For the particular etching mask thickness that we used to pattern the substrate ($\sim 11.5 \mu\text{m}$), the offset is about $2.03 \mu\text{m}$.
- **Photoresist taper.** We measured the sidewall slope of the thick resist $6 \mu\text{m}$ thick that we used in the process flow by die-sawing dummy wafers part of the process flow. We found that the sidewall angle is about 65° . Therefore, the offset due to photoresist taper is estimated at $2.8 \mu\text{m}$.
- **Photoresist resolution.** It is our experience that the MFS uncertainty for a thick resist film like those we used for the process flow of the assembly structure is about $2-3 \mu\text{m}$ (contact photolithography)

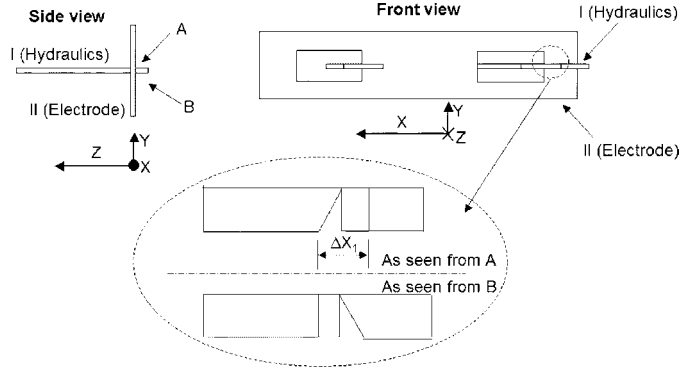


Fig. 20. ΔX measurement. The assembled test structure brings together the hydraulics substrate (I) and the electrode (II). First, the optics are set looking at the top of the device at a 45° angle (A). We need to tilt the assembly to have access to the tapered edges of both substrates from the same point of view. After this is done, we aligned the assembly so that the x -axis was parallel to one of the axes of the microscope stage. Then, we measured the distance between the two edges of the tapered edges that are not making direct contact. This offset is ΔX_1 .

- **Optical mask resolution.** Our mask was made by Advanced Reproductions (Andover, MA). This company certifies that their contact photolithography optical masks, if master pattern-generated, have a resolution of about $0.5 \mu\text{m}$.

Some of these effects occur randomly; some others occur in a deterministic/systematic way. We believe that the resolution uncertainties and the DRIE roughness occur randomly. If a Gaussian distribution is assumed, then the upper bound of these combined effects is about $3.2 \mu\text{m}$ (clearly dominated by the photolithography resolution). The RIE and photolithography tapers add up to $4.8 \mu\text{m}$. Therefore, the combined effect is about $8 \mu\text{m}$. What is left to estimate is the effect of the DRIE taper on the offset. In order to estimate this effect, we ask the reader to keep in mind that in measuring the misalignment of the assembly, we used the particular definition that we described because of the intended application, and that ideally we would like straight sidewalls. As can be seen in Fig. 20, the X -axis misalignment is controlled by the DRIE sidewall angle of both substrates (this is the only case of the three DOFs where a tapered wall interacts with another tapered wall). One of the DRIE sidewall slopes is equal to 87.5° , while the other sidewall slope is equal to 85.5° . Given the dimensions of the test structure, the ΔX due to DRIE, evaluated at the midpoint of the two substrates is bounded by

$$\Delta X = \frac{300}{\tan(87.5)} + \frac{300}{\tan(85.5)} = 36.71 \mu\text{m}. \quad (8)$$

This misalignment, combined with the other effects, makes the upper bound to be $44.5 \mu\text{m}$ for ΔX .

The DRIE processing does not affect the Y -axis misalignment because the sidewall slope is the same on opposite surfaces of the same trench (the electrode trench widens symmetrically with respect to the electrode slot width). The upper bound of misalignment is then $8 \mu\text{m}$, the estimate that we proposed for all the other offset effects.

Finally, the DRIE-related Z -axis misalignment is controlled by the springs patterned in the hydraulic body. The springs have

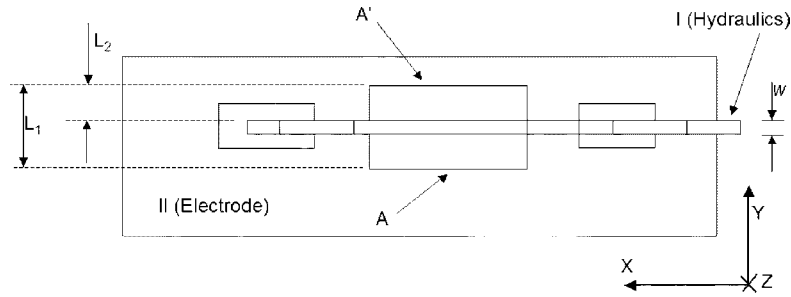


Fig. 21. ΔY measurement. The assembled test structure brings together the hydraulics substrate (I) and the electrode (II). For this particular measurement, the assembly uses electrodes with a slot width larger than the main body substrate thickness w . We rotated the structure 90° , so that the optical axis of the microscope was parallel to the normal of the plane defined by the electrode. We measured the thickness of the main body substrate with a micrometer, then the electrode slot width (L_1), and then the gap between the electrode slot boundary and the main body edge (L_2). Based on these data, we can tell the offset between the midpoint of the slot and the main body thickness. We made the assumption that the DRIE taper on both sides of the electrode slot (A, A') is the same, so the offset does not change through the electrode thickness. We verified this assumption by looking at the DRIE profiles of die-sawed samples.

a sidewall slope equal to 87.5° . Therefore, the misalignment evaluated at the midpoint in the Z -direction is bounded by

$$\Delta Z = \frac{300}{\tan(87.5^\circ)} = 13.1 \mu\text{m}. \quad (9)$$

This misalignment, combined with the other effects, makes the upper bound to be about $21 \mu\text{m}$. If the taper of the front side of the spouts is taken into account, then the bound for the DRIE misalignment in the z -direction is given by (8) because the taper of the front side of the spout is also 85.5° .

As a summary, the ΔZ and ΔX estimates are about 15% off from the measured values. There is a qualitative agreement on the ΔY misalignment between our estimate and the measurement (50% off). In any case, the test structure was successful in assembling the two substrates within the requirements of the device.

B. Misalignment Floor

We can reduce the effects of some of the sources of dimensional uncertainty that we believe produce misalignment. The following is a list of what we consider is the lower bound of the misalignment of a structure that uses the same thickness of wafers, implementing the idea of mesoscaled springs.

- *DRIE roughness.* We think that the order of magnitude of the DRIE roughness should still be around $1 \mu\text{m}$.
- *DRIE taper.* If the etching window widths are reduced, for example, by putting dummy features inside the etching trenches (the etch uniformity would be improved as well if a single window width is used in all the layout), then the influence of the DRIE taper can be reduced. We have experimental evidence that DRIE sidewalls can be as steep as 89.5° , thus producing an offset of about $2.6 \mu\text{m}$ for the midpoint of a wafer $600 \mu\text{m}$ thick.
- *RIE taper (etching mask).* If a thin aluminum etching mask is used instead of thick oxide films, the DRIE patterning should be feasible while substantially reducing the magnitude of the etching mask taper. For a submicrometer aluminum film, this value should be smaller than about $0.5 \mu\text{m}$.
- *Photoresist taper.* The aluminum film can be patterned with wet etching, very selective to photoresist. Therefore,

we can use $1\text{-}\mu\text{m}$ -thick resist to transfer the DRIE layout to the aluminum film. The measured sidewall slope of a $1\text{-}\mu\text{m}$ -thick resist film is 67° . Therefore, the offset due to photoresist taper is estimated at $0.5 \mu\text{m}$.

- *Photoresist resolution.* It is our experience that the MFS uncertainty for a thin resist film like the one we proposed for patterning the aluminum film is about $1 \mu\text{m}$ (contact photolithography).
- *Optical mask resolution.* The magnitude of $0.5 \mu\text{m}$ for a contact photolithography optical mask should be kept constant from the original analysis.

The randomly occurring dimensional variation sources add up to $1.5 \mu\text{m}$; the systematic offsets add up to $3.6 \mu\text{m}$. We suggest the lower bound of this assembly method to be around $5.1 \mu\text{m}$ in one direction, or $7.2 \mu\text{m}$ in two directions. This lower bound seems to be consistent with the misalignment average value of $10.2 \mu\text{m}$ in two directions that we obtained on structures that implement in their processes all the resolution improvements that we proposed [20].

VI. CONCLUSION

We have introduced a novel hand-assembly technique that relies on mesoscale DRIE patterned springs. The technique is suitable for certain MEMS that require effective spatial interfacing between mesoscale and microscale features, or in cases where the device is composed of subsystems whose process flows are not compatible, and that can tolerate the level of misalignment induced by the mesoscaled spring clusters. We have illustrated the packaging technique with a test structure that assembles two substrates perpendicularly to each other. The proposed design example was modeled and tested. Agreement between 3-D finite-element simulations and a simple reduced order model has been shown. The test structure demonstrated that the mesoscaled spring system can provide appropriate alignment (less than $60 \mu\text{m}$ of misalignment in a particular direction) to the device that the test structure is intended. The average misalignment in the particular direction that could seriously threaten the performance of the device was estimated at $16.34 \mu\text{m}$. Based on the metrology of the test structures, the misalignment of the proposed technique is estimated to be a few tens of micrometers along each principal direction, with a floor around $5 \mu\text{m}$ per axis—about $7 \mu\text{m}$ of biaxial misalignment.

ACKNOWLEDGMENT

The authors would like to express their gratitude to the staff of the Micro-Fabrication Technologies Laboratory, MIT, for their help on the fabrication of the test structures.

REFERENCES

- [1] S. A. Campbell, *The Science and Engineering of Microelectronic Fabrication*. Oxford, U.K.: Oxford Univ. Press, 1996.
- [2] M. J. Madou, *Fundamentals of Micro-Fabrication*, 2nd ed. Boca Raton, FL: CRC Press, 2002.
- [3] M. D. Levenson, "Phase-shifting mask strategies: Isolated dark lines," *Microolithogr. World*, vol. 6, pp. 6–12, 1992.
- [4] M. Fritze *et al.*, "Sub 100-nm krF lithography for complementary metal-oxide-semiconductor circuits," *J. Vac. Sci. Technol.*, vol. B17, pp. 245–249, 1999.
- [5] W. A. Kern, "Chemical etching," in *Thin Film Processing*, J. L. Vossen, Ed.. New York: Academic, 1978.
- [6] D. M. Manos and D. L. Flam, Eds., *Plasma Etching: An Introduction*. Boston, MA: Academic, 1989.
- [7] W. Kern, "Chemical etching of silicon, germanium, gallium arsenide, and gallium phosphide," *RCA Rev.*, vol. 39, pp. 278–308, 1978.
- [8] H. Lehr, "The LIGA technique (commercial brochure)," . Mainz-Hetchsheim, Germany, IMM Institut für Mikrotechnik GmbH, 1995.
- [9] R. Angelo and , IBM, "Photocurable epoxy composition with sulfonium salt photoinitiator," U.S. 5 102 772, 1992.
- [10] A. Bertsch *et al.*, "3D micro-fabrication by combining microstereolithography and thick resist UV photolithography," *Sens. Actuators A*, vol. 73, pp. 14–23, 1999.
- [11] X. Zhao *et al.*, "Fabrication of three-dimensional micro-structures: Microtransfer molding," *Adv. Mater.*, vol. 8, pp. 837–840, 1996.
- [12] R. J. Jackman *et al.*, "Fabrication of three-dimensional microstructures by electrochemically welding structures formed by microcontact printing on planar and curved substrates," *J. Microelectromech. Syst.*, vol. 7, 1998.
- [13] M. Shimbo *et al.*, "Silicon-to-silicon direct bonding method," *J. Appl. Phys.*, vol. 60, pp. 2987–2989, 1986.
- [14] W. H. Ko *et al.*, "Bonding techniques for microsensors," in *Micro-Machining and Micro-Packaging of Transducers*. Amsterdam, The Netherlands: Elsevier, 1985.
- [15] H. Han, "Micro-mechanical velcro," *J. Microelectromech. Syst.*, vol. 1, pp. 37–43, 1992.
- [16] A. H. Slocum, "Precision passive mechanical alignment of wafers," *J. Microelectromech. Syst.*, vol. 12, pp. 826–834, 2003.
- [17] C.-H. Cheng, "Electrical through-wafer interconnects for integrated sensors and actuators," Ph.D. dissertation, Stanford Univ., Stanford, CA, 2004.
- [18] R. M. Bostock, "Silicon nitride micro-clips for the kinematic location of optic fibres in silicon V-shaped grooves," *J. Micromech. Microeng.*, vol. 8, pp. 343–360, 1998.
- [19] C. Strandman, "Passive and fixed alignment of devices using flexible silicon elements formed by selective etching," *J. Micromech. Microeng.*, vol. 8, pp. 39–44, 1998.
- [20] B. Gassend, L. F. Velásquez, A. I. Akinwande, and M. Martínez-Sánchez, "Mechanical assembly of electrospray thruster grid," in *Proc. 29th Int. Electr. Propulsion Conf. (IEPC 2005-101)*, Princeton, NJ, 2005.
- [21] L. F. Velásquez-García *et al.*, "A micro-fabricated linear array of electrospray emitters for thruster applications," *J. Microelectromech. Syst.*, vol. 15, pp. 1260–1271, Oct. 2006.
- [22] M. Paine and S. Gabriel, "A micro-fabricated colloidal thruster array," in *Proc. 37th AIAA/ASME/SAE/ASEE Joint Propulsion Conf. Exhib. (AIAA-2001-3329)*, Salt Lake City, UT, Jul. 8–11, 2001.
- [23] A. Genovese, M. Tajmar, N. Buldrini, M. Scheerer, E. Semerad, and W. Steiger, "Indium FEPP multiemitter development and test results," in *Proc. 40th AIAA/ASME/SAE/ASEE Joint Propulsion Conf. Exhib. (AIAA-2004-3620)*, Fort Lauderdale, FL, Jul. 11–14, 2004.
- [24] M. Tajmar, "MEMS indium FEPP thruster: Manufacturing study and first prototype results," in *Proc. 40th AIAA/ASME/SAE/ASEE Joint Propulsion Conf. Exhib. (AIAA-2004-3620)*, Fort Lauderdale, FL, Jul. 11–14, 2004.
- [25] L. Dvorson, M. Ding, and A. I. Akinwande, "Analytical electrostatic model of silicon conical field emitters—Part II: Extension to devices with focusing electrode," *IEEE Trans. Electron Devices*, vol. 48, pp. 144–148, Jan. 2001.
- [26] ———, "Analytical electrostatic model of silicon conical field emitters—Part II: Extension to devices with focusing electrode," *IEEE Trans. Electron Devices*, vol. 48, Jan. 2001.
- [27] G. P. Sutton, *Rocket Propulsion Elements*. New York: Wiley, 2001.
- [28] D. U. Zhaohui, "Elemental analysis with quadrupole mass filters operated in higher stability regions," *J. Anal. Atom. Spectr.*, vol. 14, no. 8, pp. 1111–1119, 1998.
- [29] R. E. March, *Quadrupoles Storage Mass Spectrometry*. New York: Wiley, 1998.
- [30] R. A. Syms, "Design of a micro-engineered electrostatic quadrupole lens," *IEEE Trans. Electron Devices*, vol. 45, pp. 2304–2311, 1998.
- [31] S. Senturia, *Microsystem Design*. Norwell, MA: Kluwer Academic, 2000.
- [32] M. Spearing, "Controlling and testing fracture strength of silicon on the mesoscale," *J. Amer. Ceram. Soc.*, vol. 83, no. 6, pp. 1476–1484, 2000.
- [33] S. Timoshenko, *Mechanics of Materials*, 2nd ed. Boston, MA: PWS, 1984.
- [34] C. Wilson, *Computer Integrated Machine Design*, 1st ed. Upper Saddle River, NJ: Prentice Hall, 1997C. Wilson, , 1997.
- [35] W. R. Rice, "The effect of grinding direction on flaw character and strength of single crystal and polycrystalline crystals," *J. Mater. Sci.*, vol. 16, pp. 853–862, 1981.
- [36] F. W. Sears, *University Physics*, 3rd ed. Reading, MA: Addison-Wesley, 1964.



Luis Fernando Velásquez-García received the Mechanical Engineer degree (Valedictorian of the School of Engineering, *magna cum laude*) and the Civil Engineer degree (Valedictorian of the School of Engineering, *magna cum laude*) from Los Andes University, Bogotá, Colombia, in 1998 and 1999, respectively. He received the M.Sc. degree in aeronautics and astronautics and the Ph.D. degree in space propulsion from the Department of Aeronautics and Astronautics, Massachusetts Institute of Technology (MIT), Cambridge, in 2001

and 2004, respectively.

He was a Postdoctoral Associate (2004) with the Microsystems Technology Laboratories and the Gas Turbine Laboratory, MIT. Since 2005, he has been a Research Scientist there. His research focuses on micro- and nanofabrication technologies applied to propulsion, structures, and power systems. He has conducted research in micro- and nanotechnology applied to electrospray arrays, mass spectrometry, field emission, mass/charge sensors, 3-D packaging, electron impact ionization, field ionization, plasma-enhanced chemical vapor deposition carbon nanotube-based devices, turbomachinery, and chemical lasers.



Akintunde Ibitayo Akinwande (M'00) received the B.Sc. degree in electrical and electronic engineering from the University of Ife, Ife, Nigeria, in 1978 and the M.S. and Ph.D. degrees in electrical engineering from Stanford University, Stanford, CA, in 1981 and 1986, respectively.

He joined the Honeywell Technology Center, Bloomington, MN, in 1986, where he initially conducted research on GaAs complementary field-effect transistor technology for very-high-speed signal processing. He later joined the Si Microstructures Group, where he conducted research on pressure sensors, accelerometers, thin-film field emission, and display devices. He joined the Microsystems Technologies Laboratories, Massachusetts Institute of Technology (MIT), Cambridge, in 1995, where his research focuses on device and microfabrication technologies with particular emphasis on smart displays, large-area electronics, field emission and field ionization devices, and electric propulsion. He is currently a Professor in MIT's Electrical Engineering and Computer Science Department. He has received four patents in MEMS and display technologies and has authored more than 50 journal publications. He has served on a number of technical program committees for various conferences, including the Device Research Conference, the International Electron Devices Meeting, the International Solid-State Circuits Conference, the International Display Research Conference, and the International Vacuum Microelectronics Conference.

Professor Akinwande received the 1996 NSF Career Award.



Manuel Martínez-Sánchez received the Aeronautical Engineer's degree from Polytechnic University of Madrid, Spain, in 1967 and the Ph.D. degree from the Massachusetts Institute of Technology (MIT), Cambridge, in 1973.

He is currently a Professor in the Department of Aeronautics and Astronautics, MIT. His research and teaching are concentrated on space propulsion after having in the past looked into MHD power generation and other energy-related topics. He has authored about 30 journal papers and 120 conference papers.

Prof. Martínez-Sánchez is a Corresponding Member of the Spanish Academy of Engineering.